Assessment of preliminary results of baseline high entropy alloys manufactured at INL

INL/RPT-24-79358
Revision 0

Additive Manufacturing of High Entropy Alloys for Nuclear Applications Project under the Advanced Materials and Manufacturing Technologies Program

M3CR-23IN0402012 Milestone Report

JULY 2024

Michael McMurtrey,
Priyanshi Agrawal,
Crewse Petersen, and
Michael Moorehead,

Idaho National Laboratory

Idaho National Laboratory

INL/RPT-24-24-79358
Revision 0

Assessment of preliminary results of baseline high entropy alloys manufactured at INL

M3CR-23IN0402012

Michael McMurtrey,
Priyanshi Agrawal,
Crewse Petersen, and
Michael Moorehead,
Idaho National Laboratory

July 2024

Idaho National Laboratory
Idaho Falls, Idaho 83415

http://www.inl.gov

Prepared for the
U.S. Department of Energy
Office of Nuclear Energy
Under DOE Idaho Operations Office
Contract DE-AC07-05ID14517

Page intentionally left blank

SUMMARY

Materials development is needed to support the design and deployment of advanced nuclear reactors that will operate at higher temperatures and in harsher environments than the current light water reactor fleet. High entropy alloys have been identified as a class of alloy that could address the needs of advanced reactors, such as the molten salt reactors, due to their potential strength, radiation resistance, and corrosion resistance. This project summarizes the work done in fiscal year 2024 for the Additive Manufacturing of High Entropy Alloys for Nuclear Applications Project. This work has focused on examination of potential alloy compositions, down selection based on simulated results, and preliminary testing of down selected alloys.

Page intentionally left blank

ACKNOWLEDGMENTS

This work is funded under the United States Department of Energy Office of Nuclear Energy's Advanced Materials and Manufacturing Technologies Program.

Page intentionally left blank

CONTENTS

FIGURES

TABLES

Page intentionally left blank

ACRONYMS

ATR	Advanced Test Reactor
BCC	Body Centered cubic
CR	Czech Republic
DOE	Department of Energy
DOE-ID	Department of Energy-Idaho Operations Office
EBSD	Electron backscatter diffraction
EDS	Electron dispersive spectroscopy
EFAS	Electric Field Assisted Sintering
FCC	Face centered cubic
HEA	High Entropy Alloy
INL	Idaho National Laboratory
IPF	Inverse Pole Figure
MFC	Materials and Fuels Complex
MSR	Molten Salt Reactor
MSRE	Molten Salt Reactor Experiment
R&D	Research and Development
SS	Stainless steel
US	United States

Page intentionally left blank

Assessment of preliminary results of baseline high entropy alloys manufactured at INL

M3CR-23IN0402012

1. INTRODUCTION

The Additive Manufacturing of High Entropy Alloys for Nuclear Applications Project is a joint project funded by the United States (US) Department of Energy and the Technology Agency of the Czech Republic (CR). Idaho National Laboratory is leading and performing the work for the US project, collaborating closely with ÚJV Řež a.s., who leads the Czech Republic project. Charles University is supporting the CR project through alloy design, COMTES FHT will be additively manufacturing material, which will be shared with INL, and Centrum výzkumu Řež is performing precharacterization, corrosion exposure, irradiation and post-irradiation examination for the CR material. For this project, INL will be developing and testing materials manufactured through arc melting and powder metallurgy, which will help serve as a baseline for when additively manufactured materials are tested, as well as performing molten salt corrosion experiments and ion irradiations for both the US and CR materials.

The goal of this project is to increase understanding of a potential alloy system for use as a structural material for advanced nuclear reactors. Structural materials used in generation IV reactors, like the molten salt reactor (MSR), face harsh conditions (elevated temperatures, corrosive environments, irradiation) which necessitate alloys tailored to the environment. The MSR design has a number of advantages, such as (1) in fluid fuel negates meltdown danger and can be easily drained in accident situations; (2) fission products form stable compounds with salt and will stay in the salt during accident or leak scenarios; (3) noble gases bubble out of the salt and noble metals plate out, allowing collection and disposal; (4) low pressure vessels are only needed because of the relatively higher melting points of the salts compared to water; (5) salts are better coolants compared to pressurized water, allowing for smaller heat exchangers and pumps; (6) transuranic elements can be burned as they are left in the salt (LeBlanc 2010). However, the combination of high temperatures, molten salt corrosion, and radiation damage in the MSR is difficult on many commercial nuclear alloys (Allen et al. 2008). Stainless steel alloys have been deemed unfit for MSR use because of excessive chromium dissolution (Ignatiev and Surenkov 2017). Even Hastelloy N, a Nickel superalloy specifically designed for use in the molten salt reactor experiment (MSRE), has issues with embrittlement due to fission product diffusion into grain boundaries during reactor operation (McCoy and McNabb 1972). Therefore, the continued development of new alloys which are better suited for this challenging environment is of utmost importance to improve the lifespan and safety of these new reactors.

High entropy alloys (HEAs) are a potential material class that could address the challenges of MSR structural materials. These alloys are a continuing area of innovation, especially for applications in extreme environments. HEA synthesis differs from conventional alloy development, as instead of a single primary element with alloying additions that tune performance, HEAs use 4-5 different elements in quasi-equimolar proportions (Cantor et al. 2004). This novel alloying strategy brings forth various potential compositions within the vast, largely unexplored central regions of quaternary or greater alloy phase diagrams. HEAs are often described by four “core effects” (Miracle and Senkov 2017). (1) The high entropy effect: compositional complexity (usually defined as four or more elements at near equimolar ratios) leads to an increase in configurational entropy, which can stabilize HEAs into single phase, solid solution alloys. (2) The lattice distortion effect: because of differing atomic sizes of the constituent alloying elements in the solid solution, crystal lattice distortions are more severe than standard alloys.

This can affect various material properties, such as hardness, strength, and thermal properties (Murty et al. 2014). (3) The “cocktail” effect: because of the freedom alloy designers have in choosing elements for alloying, this effect has been given a descriptive name to showcase how in mixing certain element combinations, the alloy can gain material properties greater than their individual components. (4) The sluggish diffusion effect: this effect is based on experimental data showing slower diffusion of certain tracer elements in HEAs compared to other alloys (Tsai et al. 2013). Other studies have disproved the notion that all HEAs will exhibit sluggish diffusion inherently (Dąbrowa et al. 2019), but that this can be engineered into the alloy with correct alloy composition.

These HEA effects can be leveraged for molten salt reactor applications. HEAs have shown unique irradiation resistance, often linked to sluggish diffusion of irradiation induced defects, which allows for greater recombination during the initial damage cascade and slower clustering of like-defects into larger voids and loops. El Atwani et al. found that a CrHfTaVW HEA possessed above-average irradiation resistance under dual beam ion irradiation (up to 8.5 dpa) and helium implantation at 900 °C. The alloy showed no indication of radiation-induced dislocation loops, had minimal segregation of chromium and vanadium at grain boundaries, and only slight radiation induced hardening; all much less than conventional alloys in similar conditions (El Atwani et al. 2023). Lang et al. found a correlation between compositional complexity and helium bubble size during helium implantation at 900 °C. Namely, MoNb, MoNbTa, and MoNbTaW showed decreasing average helium bubble size as compositional complexity increased (Lang et al. 2022). Sadeghilaridjani et al. tested the irradiation response of reduced activation HfTaTiVZr HEA at higher damage levels (up to 40 dpa) at room temperature compared to stainless steel (SS) 304. They found that the alloy had limited amorphization and irradiation induced microstructural changes, and that the HEA only had a ~20% increase in hardness compared to SS304 having a large embrittlement due to irradiation, with a ~50% hardness increase (Sadeghilaridjani et al. 2020). Lin et al. used molecular dynamics simulations to perform displacement cascade simulations on CoCrFeNi HEA with incident nickel ions. They found that compared to less complex systems (bulk nickel), the simulation showed that there was a higher defect recombination rate in the HEA, induced by an enhanced “thermal spike” (increased time of Frenkel pair recombination), lower thermal conductivity and smaller binding energy of interstitial defects (Lin et al. 2020). These effects can be used to explain some of the physical results seen in other studies. Lack of irradiation induced dislocation loops, reduced helium bubble size, and reduced macroscopic hardening can be attributed to slower diffusion of irradiation induced defects, allowing for greater recombination rates, less clustering of defects, and reduced defect effects on material properties. Overall, HEAs appear to have inherent radiation resistant properties that could be leveraged to increase material lifetime in the MSR and other advanced reactor concepts.

Investigations of the corrosion resistance of HEAs in molten salts are in their early stages. Refractory metal based HEAs are particularly of interest as molten salt corrosion resistant materials because many refractory metals (Nb, Mo, W, etc.) are relatively more inert in molten salt environments compared to other metals (Cr, Fe). Molten salt corrosion is unique in that instead of forming passivating oxide layers to resist corrosion, these layers are not stable because of lack of oxygen in the system or susceptibility of oxide dissolution into the salts. Therefore, corrosion is driven by thermodynamic reactions of structural metallic elements with salt elements, fuel, and impurities. More inert elements, relative to the medium used, will perform better in molten salt when paired with proper redox control. This alloying strategy has proven successful, as the low Cr content, Ni based alloy Hastelloy N, specifically developed for fueled FLiBe salt use, had minimal corrosion after the 20,000 hours exposure during the MSRE (McCoy and McNabb 1972). Some literature is available on the molten salt corrosion resistance of certain HEA systems. Patel et al. tested TaTiVWZr and HfTaTiVZr HEAs in electrochemical corrosion tests, using $MgCl_2$-NaCl-KCl salt in open air at 450 and 650 °C, comparing their corrosion resistance to SS304 and

Inconel 718. They found that TaTiVWZr showed the highest corrosion resistance at both temperatures. This was attributed to the relatively more noble elements in this alloy reducing corrosion compared to the less noble constituent elements (Cr, Fe, Ni) of the Inconel and SS304 (Patel et al. 2021). Patel et al. also did electrochemical corrosion tests of the same TaTiVWZr and HfTaTiVZr HEAs in FLiNaK at 650 C for 60 hours, compared to Inconel 718 and SS316. In this case, TaTiVWZr fared the best of the two HEAs and had a similar corrosion rate as the Inconel 718 samples. This HEA showed enrichment of the noble elements after some dissolution of the susceptible elements, which the group postulated could be a longer-term corrosion preventative mechanism (Patel et al. 2023). Ion irradiation has been shown to affect the corrosion of structural metals in many different corrosion systems, including molten salts (Schmidt 2021), but little work has been done investigating the effects of ion irradiation on HEA molten salt corrosion. To fully understand to what extent HEAs could be used for MSR applications, the effects of irradiation on corrosion must be quantified. The goal of this project is to observe the corrosion behavior of specific HEA systems with and without ion-irradiation effects to further understand HEA corrosion resistance, and whether or not these are viable structural materials for MSR use. This report outlines the tests and methods used in selecting compositions of HEAs for MSR extreme environment tests in the future.

2. MATERIALS AND MANUFACTURING

The refractory HEAs in this study are examined using Thermo-Calc. In Thermo-Calc software the microstructure of any composition can be predicted by CALculation of PHAse Diagrams (CALPHAD) simulations. Partners in the CR identified five principal elements of interest: aluminum, molybdenum, niobium, titanium, and zirconium. Potential additive elements were identified as well, namely chromium, iron, and tungsten. Single phase body centered cubic (BCC) microstructure is of interest for the work and based on the predicted microstructure the compositions given in Table 1 were down selected for the initial examination. The phase diagrams for some of the compositions are given in Figure 1. The phase diagram shown in Figure 1 (a) for Alloy 4 shows that for a wide temperature range from ~500˚C to ~2000˚C material mostly consist of BCC phase with a small fraction of particles at lower temperature. Similarly, Figure 1(b) shows phase diagram for Alloy 9 where two different BCC phases exist in the microstructure and Figure 1 (c) presents phase diagram for Alloy 10 where up to 1500˚C material shows single phase BCC microstructure.

Table 1. Down selected list of compositions for refractor HEAs (Atomic percentages listed).

Alloy #	Al	Mo	Nb	Ti	Zr	Cr	Fe	V	W
1	20	20	20	20	20	-	-	-	-
2	5	30	30	30	5	-	-	-	-
3	10	30	30	30	-	-	-	-	-
4	15	30	30	25	-	-	-	-	-
5	15	30	25	25	-	5	-	-	-
6	15	30	25	25	-	-	5	-	-
7	15	30	25	25	-	-	-	-	5
8	20	15	10	30	-	-	-	-	25
9	-	25	25	25	-	-	-	25	-
10	-	-	33.3	16.7	33.3	-	-	16.7	-

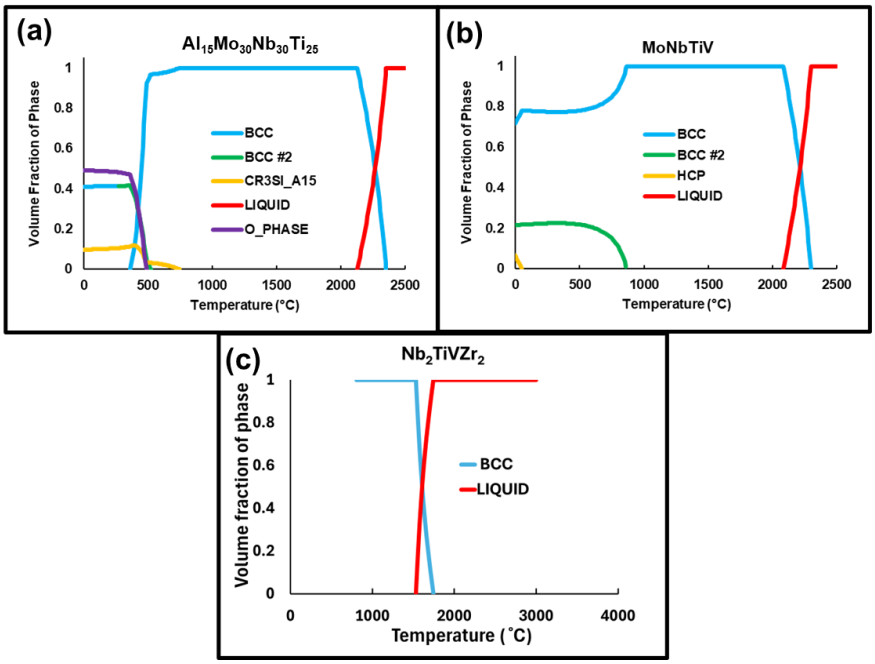

Figure 1. Phase diagrams for (a) Alloy 4, (b) Alloy 9, and (c) Alloy 10 predicted using Thermo-Calc software.

To manufacture the selected alloy compositions, an advanced manufacturing process, electric field assisted sintering (EFAS), was used. In this process, a solid compact is produced through sintering by applying heat and pressure to the starting feedstock powder. In EFAS, an electrical current is passed through the graphite die, and sometimes through the material itself, to generate heat to fuse the powder particles, generally without melting the powder. Figure 2 shows a schematic of the EFAS process used to produce HEAs in the present work. Sintered microstructures can vary from the normally arc melted microstructures of laboratory synthesized HEAs due to changes in pressure, cooling and heating between the processes (Cavaliere and Pasquale 2019). Therefore, sintered microstructure effects on irradiation and corrosion resistance must be quantified before this process can be considered for industry use.

The alloying elements are mechanically alloyed using ball milling on the feedstock before starting the EFAS process. The graph shown in Figure 3 provides the EFAS processing parameters used for sintering of refractory HEAs and Table 2 provides the heating rate used for the processing. The EFAs process gives highly dense, defect free pellets of the refractory HEAs which are difficult to process from other advanced manufacturing processes. However, the manufacturing of Nb_2TiVZr_2 alloy using EFAS process is difficult due to pyrophoricity of zirconium powder, therefore the arc melting process was used for manufacturing of Nb_2TiVZr_2 alloy in this work.

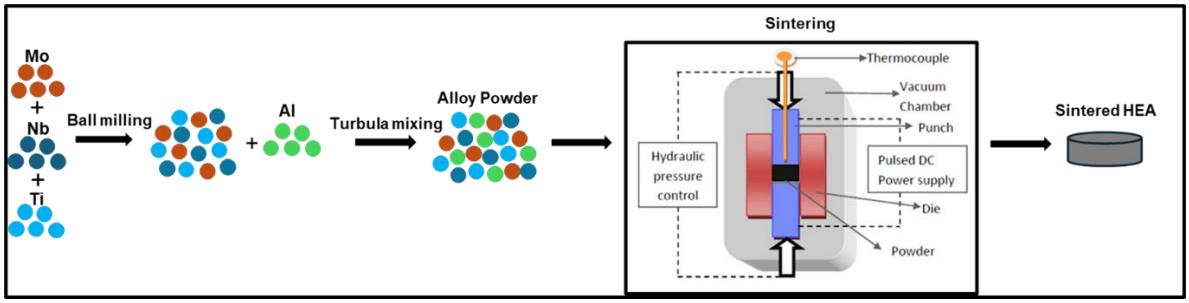

Figure 2. Schematic of sintering process for manufacturing of refractory HEA.

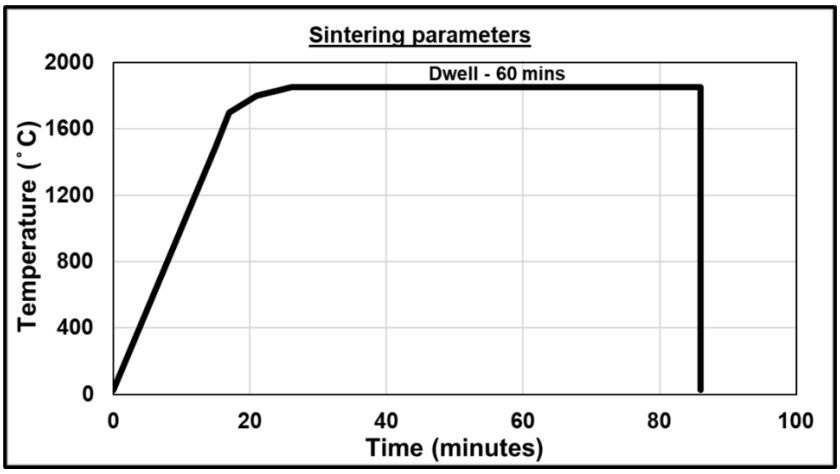

Figure 3. Process parameters for the sintering of refractory HEA.

Table 2. Heating rate during sintering of refractory HEA.

Temperature (˚C)	Heating rate (˚C / min)
1500	100
1700	50
1800	25
1850	10

3. CHARACTERIZATION

3.1. Characterization of Alloy 9 (equimolar MoNbTiV)

Figure 4 shows the back scattered scanning electron microscopy (SEM) images for sintered MoNbTiV alloy. The microstructure of as sintered material showed equiaxed grains with an average grain size of ~ 74.32 ± 24.75 µm. The formation of particles throughout the sample was also observed in the microstructure, electron dispersive spectroscopy (EDS) was performed to understand the composition of the particles in the matrix. Figure 5 shows the EDS elemental map for the sintered MoNbTiV. The EDS elemental map showed that the particles are rich in Ti and deficient in other elements.

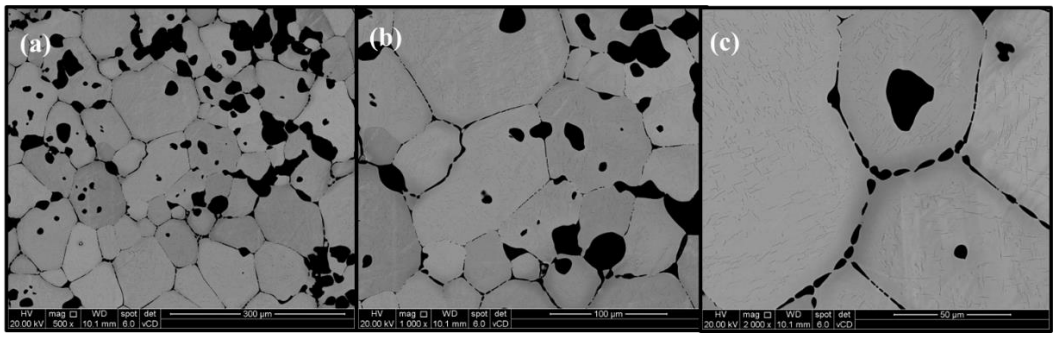

Figure 4. Back scattered SEM images for sintered MoNbVTi alloy at different magnifications.

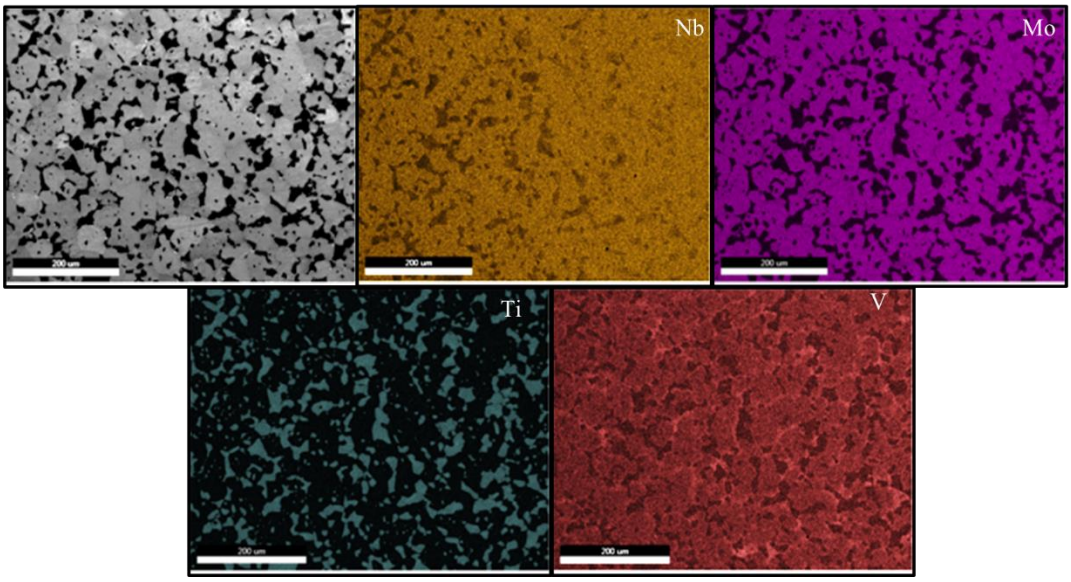

Figure 5. EDS elemental mapping for as sintered MoNbTiV alloy.

Thermal exposure tests were performed on the sintered MoNbTiV coupons to understand the thermal stability of the material. Thermal exposure tests were performed at 500˚C and 700˚C for 500 hours and 1000 hours in an argon atmosphere. Microstructural characterization was performed to understand the effect of thermal exposure on the microstructure. Figure 6 (a-b) shows the SEM images of the surface of MoNbTiV sample after 1000 hrs. at 700˚C and Figure 6 (c-d) shows cross section of the same sample. The surface of the coupon showed the formation of a dark layer with some darker particles in it. Additionally, the cross section of the coupon showed a non-uniform layer with the thickness of 50 – 100 µm, though it is not clear if this formed during the thermal exposure. The EDS analysis of the surface showed the particles are rich in Ti. The EDS elemental map for the cross-section of the material is shown in Figure 7, which shows three different types of regions near the edge of the sample: region I which has high density of Ti particles, region II is a layer rich in Ti, and region III is layer rich in Mo, Nb and V. The bulk of the sample appeared unaffected by the thermal exposure. Electron back scattered diffraction (EBSD) map of the thermally exposed material is shown in Figure 8 (a-c). The particles and the layer on the surface of the material are face centered cubic (FCC) phase and matrix is BCC phase as shown in Figure 8 (c).

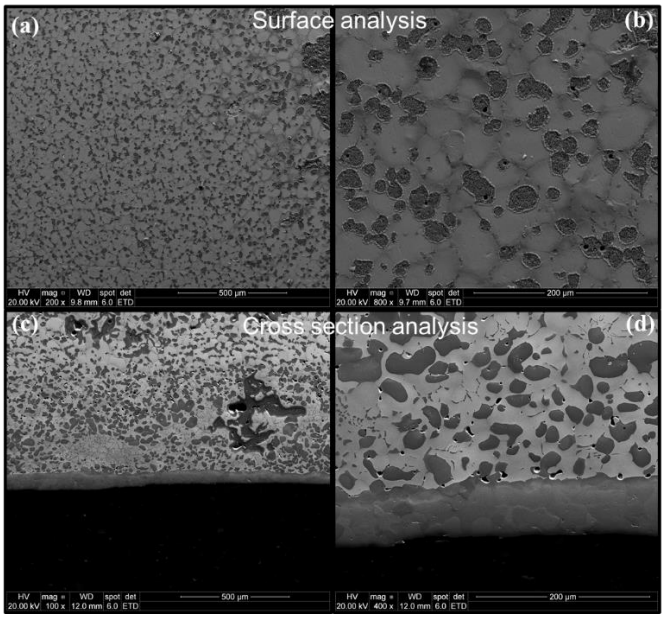

Figure 6. (a-b) SEM images for the surface of the thermally exposed MoNbTiV material at 700˚C for 1000 hrs, and (c-d) shows the SEM images for the cross-section of the thermally exposed material at 700˚C for 1000 hrs.

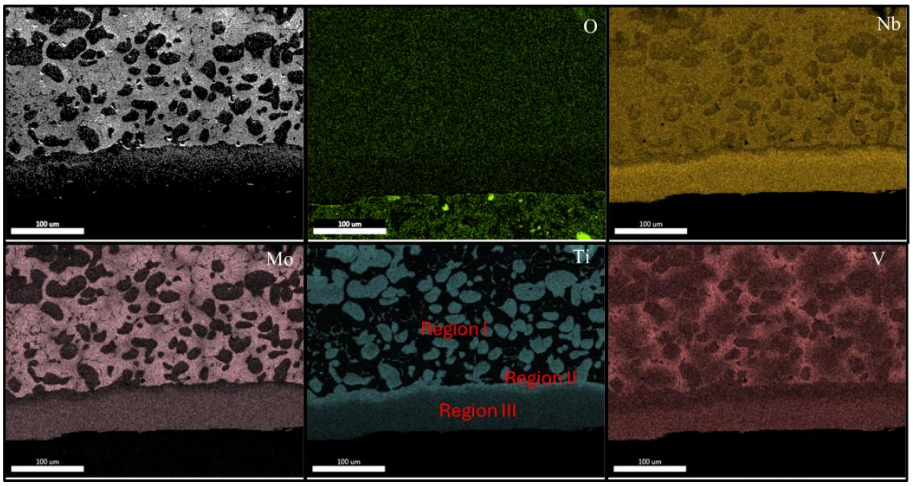

Figure 7. EDS elemental map for MoNbTiV sample thermally exposed at 700˚C for 1000 hrs.

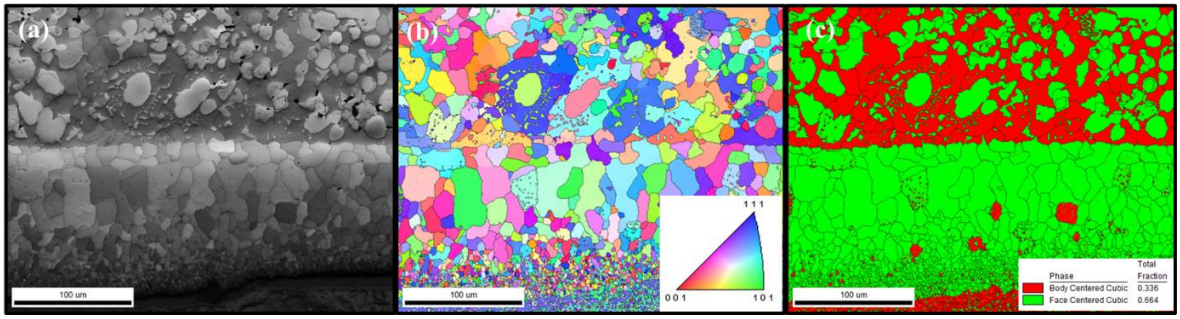

Figure 8. EBSD image quality (IQ) map, inverse pole figure (IPF) map, and phase map respectively for thermally exposed sample.

The titanium rich particles are mostly TiC, and the reason for carbon in the alloy is likely the graphite foil used for EFAS processing of the material between the die and the powder. In order to avoid formation of these TiC particles, a tungsten foil was used while manufacturing equimolar MoNbVTi samples in place of the graphite foil. Figure 9 (a-b) shows the SEM images of the sample manufactured using the tungsten foil, and the formation of particles is still observed in material. These particles are uniformly observed in the material. The EDS analysis shown in figure 9 (c-d) shows that the particles formed are rich in titanium and oxygen, rather than carbon. Oxygen is likely preexisting in the feedstock powder.

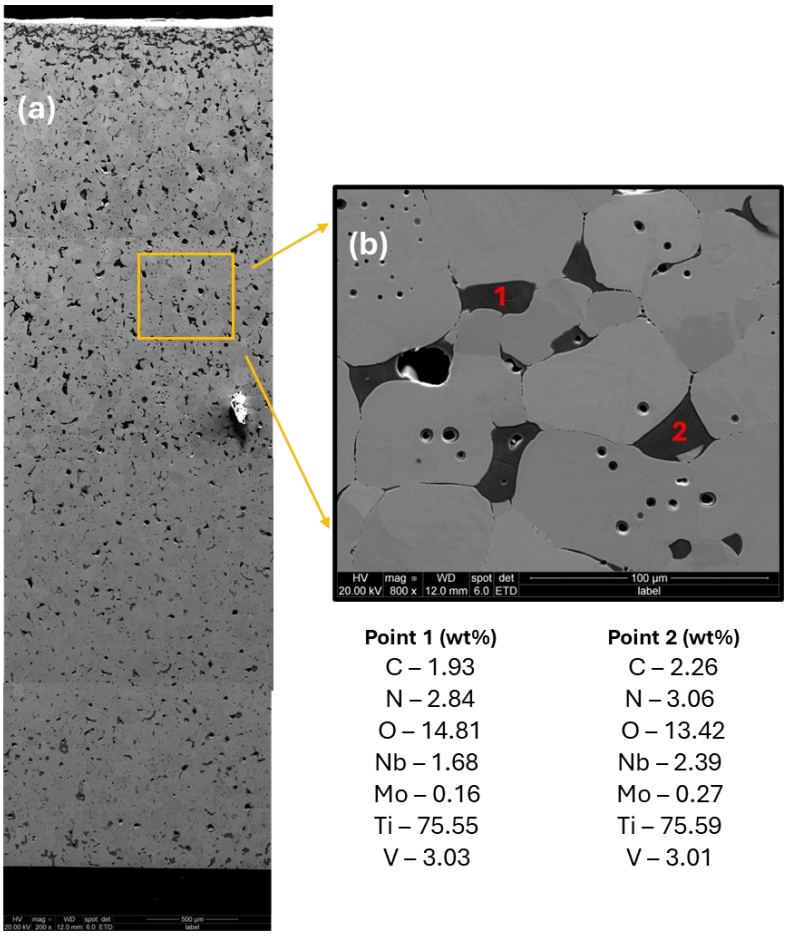

Point 1 (wt%)	Point 2 (wt%)
C – 1.93	C – 2.26
N – 2.84	N – 3.06
O – 14.81	O – 13.42
Nb – 1.68	Nb – 2.39
Mo – 0.16	Mo – 0.27
Ti – 75.55	Ti – 75.59
V – 3.03	V – 3.01

Figure 9. (a-b) SEM images of the sample manufactured using W foil, (b) EDS spot analysis of the equimolar MoNbVTi sample.

3.2. Characterization of Alloy 4 ($Al_{15}Mo_{30}Nb_{30}Ti_{25}$)

Alloy 4 was manufactured using EFAS process with the processing parameters provided in Figure 3. The microstructure of the sintered Alloy 4 is shown in Figure 10. The low magnification SEM image (Figure 10 (a)) shows formation of equiaxed grain with a high density of uniformly distributed particles in it. The average grain size for the as sintered material is 20±10 µm. EBSD IPF map (Figure 10 (b)) shows the grains in as sintered material do not have a preferential orientation and the phase map (Figure 10 (c)) shows that matrix is BCC phase whereas the particles present are TiC particles.

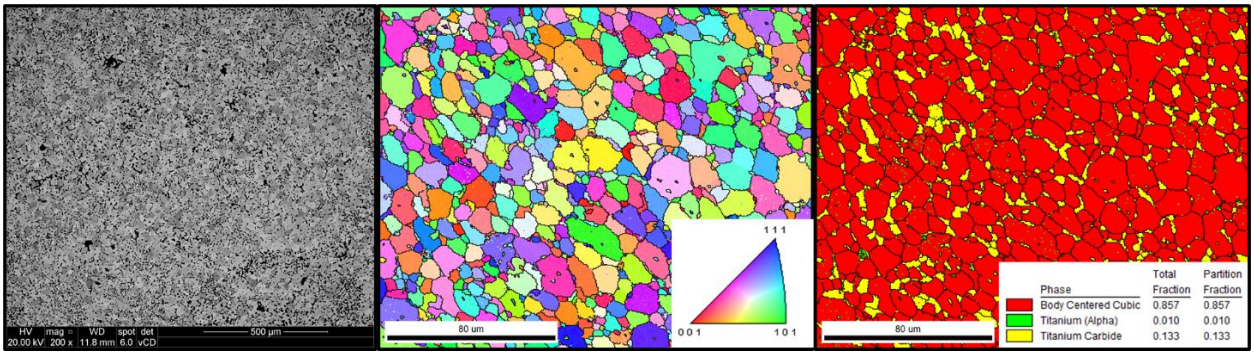

Figure 10. (a) Low magnification SEM image for the as sintered Alloy#4, (b) and (c) are IPF and phase map respectively for Alloy 4.

The EDS map for the material presented in Figure 11 shows that some particles are rich in Ti, N, and C, whereas some particles are rich in Al and O. The particles that are rich in Ti, C, and N are complex titanium carbine or nitride where particles rich in Al and O are Al2O3. The C, O and N may be introduced in the material during ball milling or may have already be present in the procured powder.

To homogenize the microstructure of the alloy, a homogenization treatment at 1200˚C for 48 hrs. was performed. Figure 12 shows the SEM images of the heat-treated sample. The precipitates were found to be stable and could not be dissolved during the homogenization treatment. The manufacturing process needed to be modified in order to reduce the formation of the carbides, nitrides, and oxides.

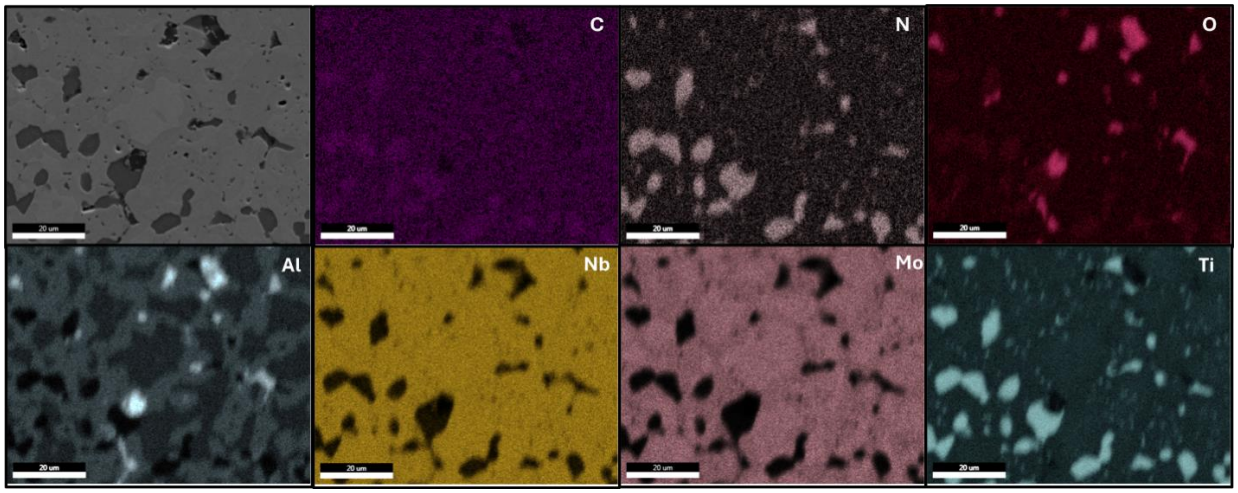

Figure 11. (a) EDS elemental map for as sintered Alloy 4.

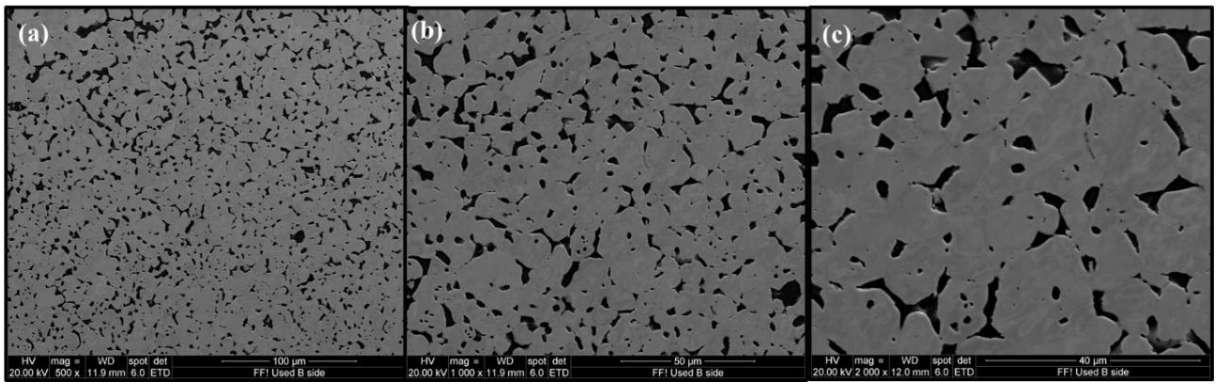

Figure 12. SEM images of the heat-treated Alloy 4.

A different sintering parameter set was used for manufacturing Alloy 4 to see the effect of sintering parameters on the microstructure of the alloy and try to reduce the formation of the precipitates. To reduce the formation of precipitates, the lowest sintering temperature that would result in full sintering of the powder was chosen. This was determined by looking at the EFAS ram position vs. temperature, as shown in Figure 13. The ram position decreases as powder consolidates and a minimum ram position occurred around 1300˚C, which indicates the point where shrinkage due to powder consolidation starts to occur more slowly than thermal expansion. The peak temperature chosen for the sintering process was 1400˚C and the sample was kept at peak temperature for 10 minutes. Figure 14 shows the SEM images of the Alloy 4 sintered at 1400˚C. The microstructure of the material comprised of very fine grains with uniformly distributed fine particles. The average grain size of the material is 4±1 µm. The EDS map for the sample is shown in Figure 15 and similar to the previous manufacturing method, the particles in this case are Ti(C/N) and Al_2O_3 as well. The lower sintering temperature did appear to reduce the size of the precipitates, and the smaller, more uniformly distributed particles likely will increase the mechanical properties of the alloy as compared to the larger particles that formed during the higher temperature sintering process.

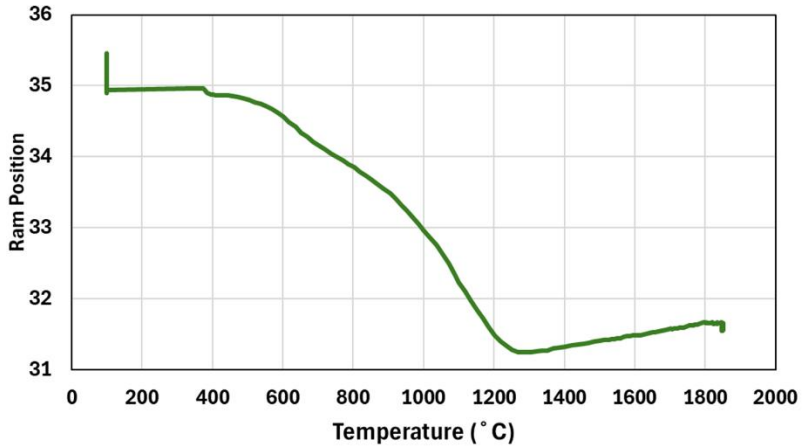

Figure 13. Ram position during EFAS sintering, related to consolidation of particles at increasing temperatures.

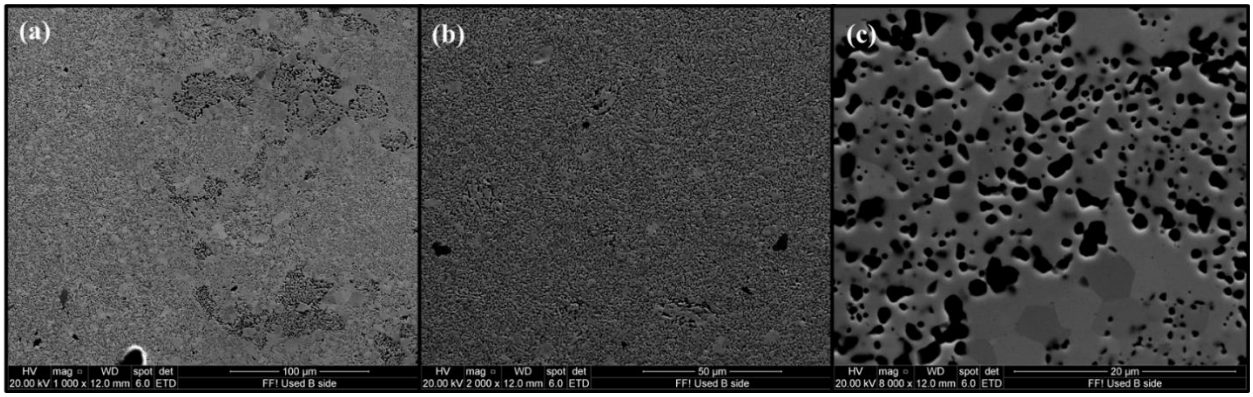

Figure 14. SEM images of the Alloy 4 processed at peak temperature of 1400˚C.

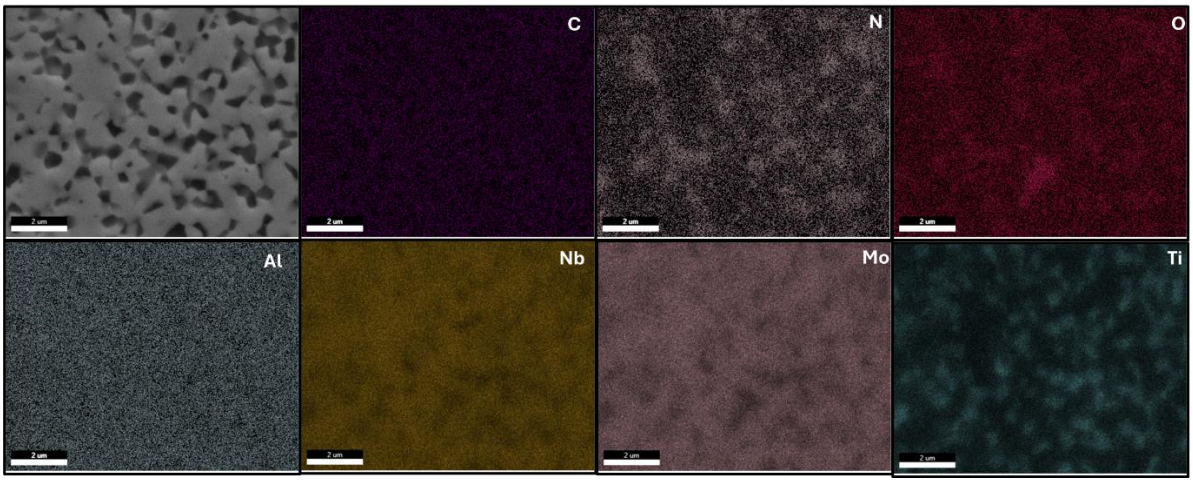

Figure 15. EDS elemental map for Alloy 4 processed at peak temperature of 1400˚C.

3.3. Characterization of Alloy 10 (Nb_2TiVZr_2)

Alloy 10 was manufactured by an arc melting process, as Zr powder is a pyrophoric and the high concentration of Zr in the Alloy 10 presented challenges with EFAS processing of the alloy. Figure 16 shows the microstructure of the arc melted Alloy 10. Figure 16 (a) shows that the material has large grains with an average grain size of 200±150 µm. The IPF map in Figure 16 (b) shows that the material does not have any preferential orientation, and the phase map (Figure 16 (c)) depicts that the material has single BCC phase microstructure.

EDS line scans (Figure 17 (a-b)) show that the alloying elements are close to the desired composition. However, the high magnification SEM image shown in Figure 17 (c) indicates that there is micro-segregation in the material. Arc melting is a solidification process and during solidification the elements with lower partition coefficients tend to segregate at the boundaries.

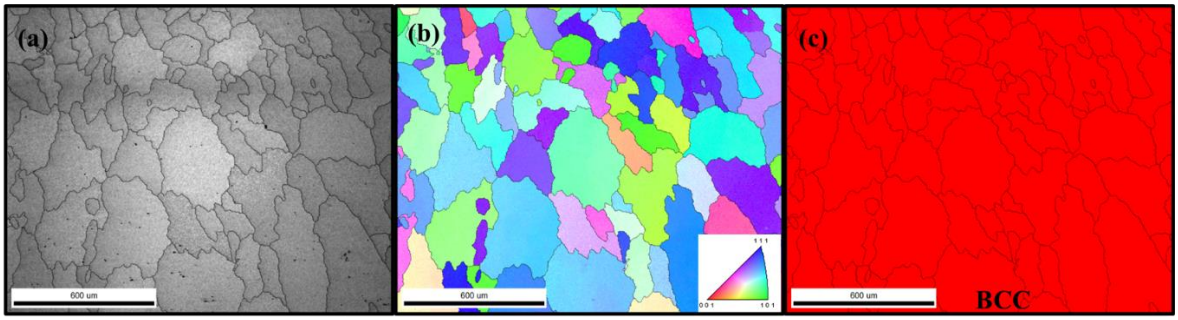

Figure 16. EBSD IQ, IPF, and phase map respectively for arc melted Alloy 10.

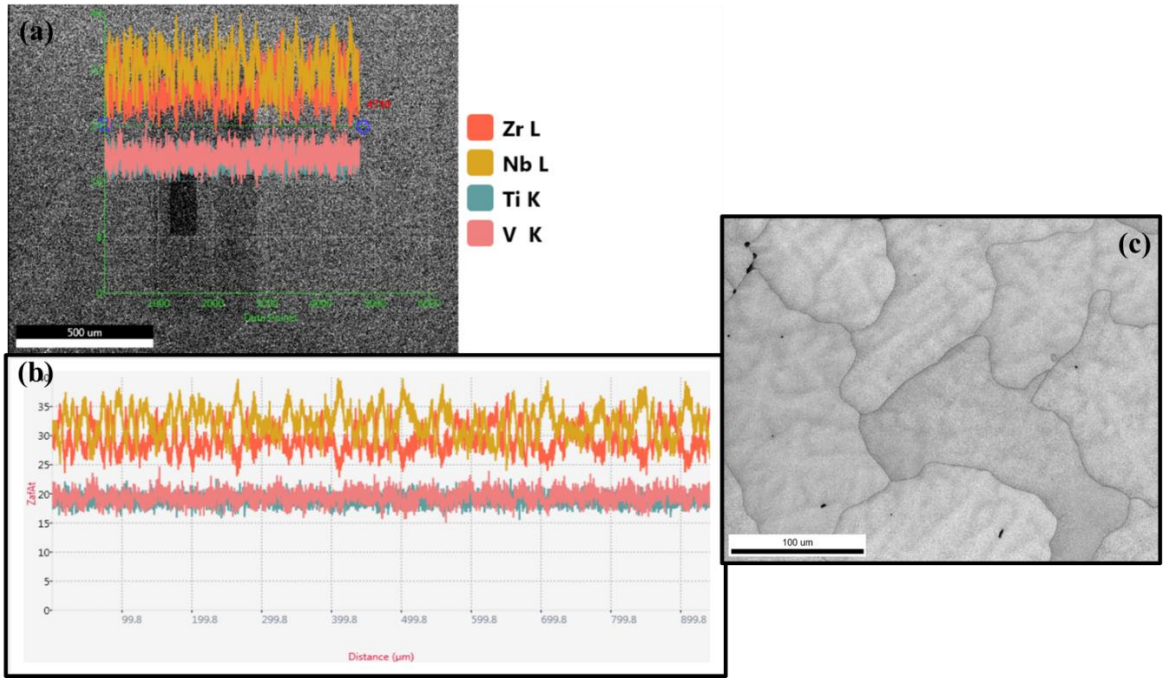

Figure 17. (a-b) EDS line scan map, (c) SEM image for arc melted Alloy 10.

4. PRELIMINARY ASSESSMENT

Of the ten compositions of interest, three were selected for manufacturing and characterization. While Alloys 4 and 9 were expected to have some secondary phases at room temperature, there were differences observed in the characterization than predicted by CALPHAD. Particularly in Alloy 9, which was expected to have two BCC phases, but instead had one BCC and one FCC phase. It seems likely that these changes in expected phases are a result of interstitial elements, such as carbon (graphite dies used in EFAS are a likely source) and oxygen (present in powders as large amounts of surface oxide due to the high surface area to volume ratio). Carbon appears to be reduced through the use of tungsten foils, however additional work will need to be performed to attempt to reduce the oxygen in the powder. Alloy 10 was found to be pure BCC and is a promising candidate to move forward in molten salt and ion irradiation testing, however, with the current setup, this alloy will need to be arc melted, and will not be usable for testing EFAS materials. Work is expected to progress in determine a safe way to work with the zirconium powder in the ball milling process to permit manufacturing of Alloy 10 with the EFAS process as well.

The finely distributed precipitates in Alloy 4 at the lower sintering temperature may not be detrimental to the strength of the material, however, there are concerns that the small grain sizes may result in poor performance at high temperatures where creep is prominent. This alloy and Alloy 9 may prove more promising once methods for reducing carbon and oxygen are both implemented, which will allow for the higher sintering temperature and larger grains. Further testing will be performed to ensure these oxides and carbides can be reduced prior to implementing a molten salt/ion irradiation test program on these alloys.

At this point, no mechanical testing has been performed, and it is not the focus of this project. However, to ensure usability of alloys that are being ion irradiated and exposed to molten salt, limited mechanical testing will be performed as well, which will help determine the extent that secondary phases are detrimental in Alloy 4, as well as other HEAs where the secondary phases are observed. In the thermal exposures performed, no significant changes were observed in the material, so changes observed during the molten salt exposures in the upcoming phase of the project are expected to be solely due to molten salt effects rather than thermal processes.

5. CONCLUSIONS

In this study, we utilized Thermo-Calc software for developing several alloys, employing CALPHAD simulations to predict phase diagrams across various compositions. Among the alloys formulated, we manufactured and characterized a subset. The EFAS processing of equimolar MoNbVTi and $Al_{15}Mo_{30}Nb_{30}Ti_{25}$ alloys resulted in the formation of titanium-rich second-phase particles within a BCC matrix. Conversely, arc melting of Nb_2TiVZr_2 led to the formation of a single-phase BCC microstructure, albeit with larger grains than observed in the other alloys, due to the melting process of the arc melter manufacturing. The primary aim of this study is to create a corrosion-resistant alloy suitable for nuclear applications. By developing alloys with different microstructures, we aim to enhance our understanding of how these features influence the material's corrosion resistance. The Nb_2TiVZr_2 alloy is now being prepared for ion irradiation and molten salt testing. Limited testing will continue for other alloys as well, which will help increase understanding of the effects of the secondary phases within the HEAs.

6. REFERENCES

Allen, T. R., K. Sridharan, L. Tan, W. E. Windes, J. I. Cole, D. C. Crawford, and Gary S. Was. 2008. "Materials Challenges for Generation IV Nuclear Energy Systems." Nuclear Technology 162 (3): 342–57. https://doi.org/10.13182/NT08-A3961.

Cavaliere, Pasquale. 2019. Spark Plasma Sintering of Materials: Advances in Processing and Applications. Springer.

Ignatiev, V., and A. Surenkov. 2017. "5 - Corrosion Phenomena Induced by Molten Salts in Generation IV Nuclear Reactors." In Structural Materials for Generation IV Nuclear Reactors, edited by Pascal Yvon, 153–89. Woodhead Publishing. https://doi.org/10.1016/B978-0-08-100906-2.00005-7.

McCoy, H.E., and B. McNabb. 1972. "INTERGRANULAR CRACKING OF INOR-8 IN THE MSRE." ORNL--4829, 4581899. https://doi.org/10.2172/4581899.

LeBlanc, David. 2010. "Molten Salt Reactors: A New Beginning for an Old Idea." Nuclear Engineering and Design 240 (6): 1644–56. https://doi.org/10.1016/j.nucengdes.2009.12.033.

Cantor, B., I. T. H. Chang, P. Knight, and A. J. B. Vincent. 2004. "Microstructural Development in Equiatomic Multicomponent Alloys." Materials Science and Engineering: A 375–377 (July):213–18. https://doi.org/10.1016/j.msea.2003.10.257.

Miracle, D. B., and O. N. Senkov. 2017. "A Critical Review of High Entropy Alloys and Related Concepts." Acta Materialia 122 (January):448–511. https://doi.org/10.1016/j.actamat.2016.08.081.

Murty, B. S., J. W. Yeh, and S. Ranganathan. 2014. "Chapter 2 - High-Entropy Alloys: Basic Concepts." In High Entropy Alloys, edited by B. S. Murty, J. W. Yeh, and S. Ranganathan, 13–35. Boston: Butterworth-Heinemann. https://doi.org/10.1016/B978-0-12-800251-3.00002-X.

Tsai, K. -Y., M. -H. Tsai, and J. -W. Yeh. 2013. "Sluggish Diffusion in Co–Cr–Fe–Mn–Ni High-Entropy Alloys." Acta Materialia 61 (13): 4887–97. https://doi.org/10.1016/j.actamat.2013.04.058.

Dąbrowa, Juliusz, Marek Zajusz, Witold Kucza, Grzegorz Cieślak, Katarzyna Berent, Tomasz Czeppe, Tadeusz Kulik, and Marek Danielewski. 2019. "Demystifying the Sluggish Diffusion Effect in High Entropy Alloys." Journal of Alloys and Compounds 783 (April):193–207. https://doi.org/10.1016/j.jallcom.2018.12.300.

El Atwani, O., H. T. Vo, M. A. Tunes, C. Lee, A. Alvarado, N. Krienke, J. D. Poplawsky, et al. 2023. "A Quinary WTaCrVHf Nanocrystalline Refractory High-Entropy Alloy Withholding Extreme Irradiation Environments." Nature Communications 14 (1): 2516. https://doi.org/10.1038/s41467-023-38000-y.

Lang, Eric, Kory Burns, Yongqiang Wang, Paul G. Kotula, Andrew B. Kustas, Sal Rodriguez, Assel Aitkaliyeva, and Khalid Hattar. 2022. "Compositional Effects of Additively Manufactured Refractory High-Entropy Alloys under High-Energy Helium Irradiation." Nanomaterials 12 (12): 2014. https://doi.org/10.3390/nano12122014.

Sadeghilaridjani, Maryam, Aditya Ayyagari, Saideep Muskeri, Vahid Hasannaeimi, Riyadh Salloom, Wei-Ying Chen, and Sundeep Mukherjee. 2020. "Ion Irradiation Response and Mechanical Behavior of Reduced Activity High Entropy Alloy." Journal of Nuclear Materials 529 (February):151955. https://doi.org/10.1016/j.jnucmat.2019.151955.

Lin, Yeping, Tengfei Yang, Lin Lang, Chang Shan, Huiqiu Deng, Wangyu Hu, and Fei Gao. 2020. "Enhanced Radiation Tolerance of the Ni-Co-Cr-Fe High-Entropy Alloy as Revealed from Primary Damage." Acta Materialia 196 (September):133–43. https://doi.org/10.1016/j.actamat.2020.06.027.

Patel, Kunjal, Maryam Sadeghilaridjani, Mayur Pole, and Sundeep Mukherjee. 2021. “Hot Corrosion Behavior of Refractory High Entropy Alloys in Molten Chloride Salt for Concentrating Solar Power Systems.” Solar Energy Materials and Solar Cells 230 (September):111222. https://doi.org/10.1016/j.solmat.2021.111222.

Patel, Kunjal, Chaitanya Mahajan, Saideep Muskeri, and Sundeep Mukherjee. 2023. “Corrosion Behavior of Refractory High-Entropy Alloys in FLiNaK Molten Salts.” Metals 13 (3): NA-NA. https://doi.org/10.3390/met13030450.

Schmidt, Franziska, Peter Hosemann, Raluca O. Scarlat, Daniel K. Schreiber, John R. Scully, and Blas P. Uberuaga. 2021. “Effects of Radiation-Induced Defects on Corrosion.” Annual Review of Materials Research 51 (1): 293–328. https://doi.org/10.1146/annurev-matsci-080819-123403.

Page intentionally left blank